OCEANOGRAPHY

Ocean alkalinity destruction by anthropogenic seafloor disturbances generates a hidden CO_2 emission

Sebastiaan J. van de Velde[1,2,3]*, Astrid Hylén[3], Filip J. R. Meysman[3]

The seafloor is responsible for 40% of the alkalinity input to the ocean, thus contributing to the ocean's capacity to sequester atmospheric CO_2. Anthropogenic seafloor disturbances induced by mobile bottom-contact fishing and dredging influence this natural carbon sink, yet the human impact on the ocean's alkalinity cycle remains poorly quantified. Model simulations show that the combined impact of mobile bottom-contact fishing (e.g., trawling) and dredging reduces natural alkalinity generation by 60 to 220 gigaequivalent year^{-1}, which is equivalent to a reduction of the natural marine carbon sink by 2 to 8 teragrams CO_2 year^{-1}. Alkalinity destruction by anthropogenic seafloor disturbance hence generates a hidden CO_2 emission, of which the impact is comparable to the estimated reduction of organic carbon burial by mobile bottom-contact fishing. Our analysis emphasizes that carbon accounting in marine systems should consider the anthropogenic impact on both the organic and inorganic carbon cycles.

INTRODUCTION

Since the start of the industrial revolution, the ocean has taken up ~25% of anthropogenic carbon dioxide (CO_2) emissions, thus alleviating the impact of ongoing global warming (*1*). CO_2 efficiently dissolves in seawater, and as a result, the ocean provides a large sink for atmospheric CO_2 (*2*, *3*). The CO_2 storage capacity of seawater is principally controlled by its alkalinity (A_T) content, which is the excess of proton acceptors (bases) over proton donors (acids) (*4*). In the geological past, ocean alkalinity feedbacks have played a vital role in regulating the Earth's climate: Periods of intense warming have resulted in intensified weathering, thus releasing additional A_T to the ocean, which traps atmospheric CO_2 and counters warming. Given the urgent need for climate stabilization, this natural feedback has inspired the idea of "ocean alkalinity enhancement" (OAE), which refers to technologies that aim to deliberately increase the A_T of the surface waters to achieve active carbon dioxide removal (CDR). OAE technologies are in an early phase of investigation, and various approaches are being proposed to achieve alkalinization, including mineral addition, electrochemistry, and liming of surface waters (*5*). However, little attention has been given to the opposite process, i.e., the possibility of anthropogenic ocean alkalinity destruction and concomitant CO_2 emissions. Anthropogenic activities like mobile bottom-contact fishing and dredging have the potential to negatively affect the natural processes that generate A_T, thereby decreasing A_T levels in the surface ocean and thus reducing its CO_2 sequestration capacity.

Marine sediments account for ~40% of the external A_T input to the ocean (~20 Tequiv A_T year^{-1}), while the remainder is due to riverine input of dissolved compounds (*6*–*8*). Most of this sedimentary A_T input (52%) is generated via the dissolution of detrital carbonates (i.e., carbonates originating from land) (*8*), while pyrite (FeS_2) formation and burial accounts for 24% and the remainder is generated by anaerobic mineralization via denitrification (nitrate reduction to N_2 gas) (8%) and organic matter burial (16%) (*7*, *9*). Because shallow marine waters are oversaturated with respect to carbonates, carbonate dissolution typically occurs within the oxygenated zone of marine sediments, where acidity is created via aerobic respiration (*10*, *11*). In contrast, denitrification and pyritization primarily occur in the anoxic part of the sediments, where anaerobic mineralization pathways dominate the decomposition of organic matter (*12*). If the sedimentary efflux of A_T to the overlying water is reduced, the A_T levels in the surface ocean will decrease, inducing a concomitant efflux of CO_2 to the atmosphere. As such, ocean alkalinity destruction essentially generates a hidden CO_2 emission from the fishing and dredging activities.

The coastal and shelf seafloor is strongly affected by various anthropogenic activities that cause sediment disturbance, such as mobile bottom-contact fishing and dredging (*13*), which are widespread and frequent activities across the global continental shelf. Around 15% of the continental shelf area down to 1000 m water depth is disturbed at least once every 5 years by bottom-contact fishing (*14*, *15*), a practice during which heavy nets and chains are dragged across the seafloor. Trawling gear typically penetrates up to 5 cm into the seafloor, leading to resuspension of particles in the water column and homogenization of the upper few centimeters of sediment. Globally, 20 to 90 Gt of sediment are resuspended annually, and up to 200 Gt of sediment deposits are homogenized (*16*). Dredging activities imply sediment excavation and subsequently redeposition in marine environments. Global sediment volumes for dredging are less well documented, but we estimate that ~2.1 Gt of sediment was relocated by dredging globally in 2021. Mobile bottom-contact fishing and dredging physically affect the seafloor and alter the natural geochemical cycles (*17*, *18*), with the potential to disrupt natural A_T generation in the seafloor. By re-exposing anoxic sediments to oxygenated water, via either resuspension or homogenization, mobile bottom-contact and dredging can stimulate FeS_2 reoxidation (*17*, *19*), leading to the removal of A_T. At the same time, the pathways of denitrification and carbonate formation/dissolution are disturbed within the sediment by the introduction of oxygen-rich overlying water, oversaturated with respect to calcite and aragonite phases, into the pore water (*17*, *20*).

To support the development of effective climate policies, an accurate assessment of the net emission or removal of CO_2 by both terrestrial and marine ecosystems is critical (*3*). While extensive knowledge

[1]Department of Marine Science, University of Otago, Dunedin, New Zealand. [2]National Institute of Water and Atmospheric Research, Wellington, New Zealand. [3]Department of Biology, University of Antwerp, Wilrijk, Belgium.
*Corresponding author. Email: sebastiaan.vandevelde@otago.ac.nz

has been built up in the terrestrial realm, marine carbon accounting is still in its early stages (*21*, *22*). Within the impact of fisheries, most research has so far focused on the impact of mobile bottom-contact fishing on the sequestration of organic carbon in the seafloor. Initial estimates suggested that mobile bottom-contact fishing could potentially cause emissions of ~500 Tg CO_2 $year^{-1}$ through the stimulation of organic carbon mineralization (*23*, *24*). Yet, subsequent assessments reveal that this provides a substantial overestimation of the organic matter oxidation effect, which is more likely on the order of ~10 Tg CO_2 $year^{-1}$ (*25*–*29*). To enable accurate carbon accounting in marine systems, the anthropogenic impact on the inorganic carbon cycle must also be properly quantified. Yet at present, there are no reliable quantitative estimates of the extent to which anthropogenic sediment disturbances effectively remove ocean A_T, and so the "indirect" CO_2 emissions resulting from ocean alkalinity destruction remain unidentified.

Here, we compiled a global dataset of in situ measured fluxes of A_T, dissolved inorganic carbon (DIC), and oxygen (O_2), and used this dataset to validate a biogeochemical model of the seafloor. We simulated the impact of mobile bottom-contact fishing and dredging on the seafloor biogeochemistry and quantified the global loss of A_T and associated marine CO_2 sequestration potential due to anthropogenic sediment disturbance.

RESULTS AND DISCUSSION

Global seafloor alkalinity release

For our global dataset, we compiled A_T ($n = 270$), DIC ($n = 251$), and O_2 ($n = 260$) fluxes across the global seafloor (fig. S1A). Flux data from cohesive sediments were categorized into four different habitats according to water depth: "coastal mud" (<50 m water depth), "shelf mud" (<200 m water depth), "slope" (<2000 m water depth), and "deep sea" (>2000 m water depth). Flux data from permeable sediments were placed into a single category ("coastal and shelf sand"), as there were less than 10 data points from water depths <50 m and none above >200 m. This data compilation reveals that, per area, coastal muds provide the highest A_T release with an average flux of 12.4 mequiv A_T m^{-2} day^{-1} ($n = 83$) (Fig. 1A). Muddy shelf areas generate ~2.4 mequiv A_T m^{-2} day^{-1} ($n = 55$), while slope and deep-sea sediments generate <1 mequiv A_T m^{-2} day^{-1} (Fig. 1A), and sandy sediments generate 5.7 mequiv A_T m^{-2} day^{-1} ($n = 18$) (Fig. 1A). DIC and O_2 fluxes follow the same trend as the A_T flux (Fig. 1A), thus signifying the role of organic matter decomposition in A_T generation. Organic matter mineralization and carbonate dissolution produce DIC, and so a sediment with higher metabolic activity and total O_2 uptake is expected to display a higher DIC and A_T efflux. Likewise, carbonate dissolution, denitrification, and pyrite precipitation are all driven by heterotrophic microbial activity in the sediment, which in turn determines the sedimentary O_2 uptake (*6*, *30*). The observed variation in measured fluxes within each habitat and depth category is caused by local differences in temperature, organic matter supply, and calcium carbonate supply.

We developed a one-dimensional biogeochemical model that combines physical and biological transport in the seafloor with a state-of-the-art pore-water pH description (*31*). The reaction network embedded in the model includes all relevant A_T-producing and consuming processes in a marine sediment: aerobic respiration, denitrification, sulfate reduction, pyrite precipitation, carbonate dissolution, and precipitation. The model is able to reproduce the observed trends in A_T, DIC, and O_2 fluxes and carbonate dissolution rates by

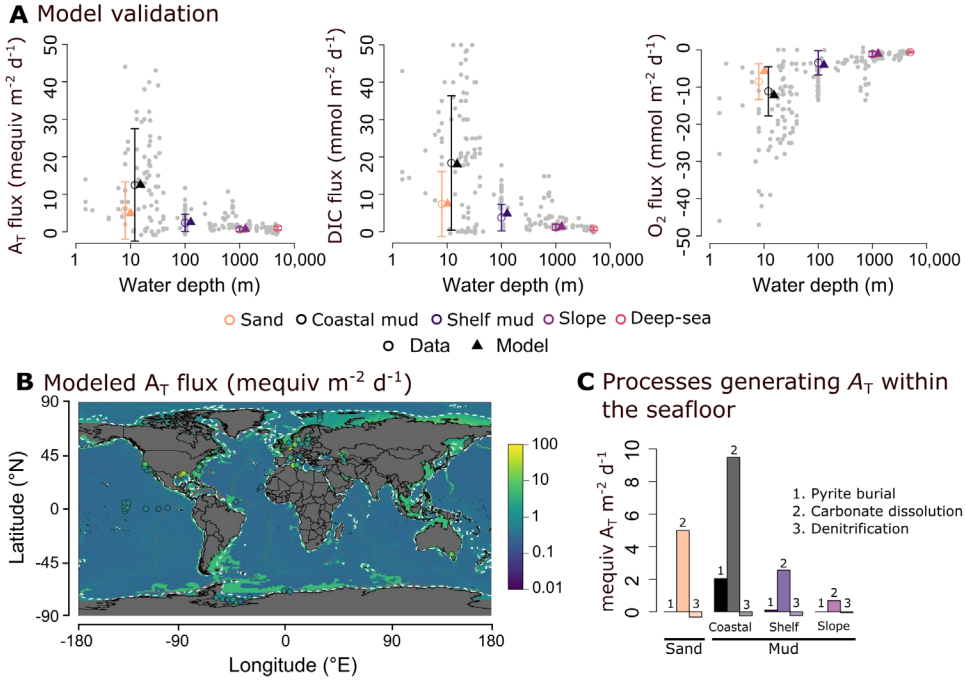

Fig. 1. Natural seafloor alkalinity (A_T) generation. (**A**) Model-data comparison of benthic fluxes (diffusive + advective) of A_T, dissolved inorganic carbon (DIC), and oxygen (O_2). Gray dots indicate individual data points, and colored dots are mean values with SD. (**B**) Modeled seafloor A_T fluxes. Dashed white lines indicate 1000-m water depth (the depth down to which the seafloor is affected by mobile bottom-contact fishing regularly). Individual data points are plotted as dots. (**C**) Contribution of individual pathways to the sedimentary A_T generation. Simulated pore-water profiles are shown in fig. S2.

varying the input of organic carbon and carbonates between the five seafloor environments (sand $R^2 = 0.43$, coastal mud $R^2 = 0.43$, shelf mud $R^2 = 0.48$, slope $R^2 = 0.18$; fig. S1B), as these inputs are known to strongly depend on water depth (*32*, *33*) (Fig. 1A). We subsequently used our model-derived relation between seafloor A_T generation, water depth, and sediment type to derive a global map of seafloor A_T fluxes (Fig. 1B). The habitats with the highest A_T efflux are located on the continental shelves, which are also the ocean zones that host the most intensive anthropogenic activities (*34*).

The model simulations reveal that most A_T is generated through carbonate dissolution, accounting for 80% of the A_T efflux from coastal muddy sediments and up to 100% in slope sediments (Fig. 1C), in accordance with field observations and previous model estimates (*6*, *35*, *36*). Across the coastal, shelf, and slope seafloor, 54 Tequiv A_T year^{-1} is generated through carbonate dissolution, which is slightly higher than the dissolution rate derived from the difference between carbonate production and burial on the shelf and slope (10 to 34 Tequiv A_T year^{-1}) (*10*). Note that the modeled carbonate dissolution rate also includes the dissolution of biogenic carbonates formed within marine ecosystems. The dissolution of these carbonates should not be considered an external A_T source to the ocean, as A_T was consumed during their formation. The subsequent dissolution of marine carbonate in the sediment comprises internal recycling and does not lead to a net A_T gain. Consequently, the global net contribution of carbonate dissolution to the marine A_T budget is limited by the input of detrital carbonate minerals from land (estimated at 10 Tequiv A_T year^{-1}) (*8*). Our model analysis also suggests that net denitrification does not substantially contribute to the sedimentary A_T input to the ocean. Instead, the production of ammonium from organic matter mineralization and its subsequent oxidation to nitrate is always larger than the reduction of nitrate to N_2 (Fig. 1C). This negligible contribution of denitrification to sedimentary A_T generation is in line with existing estimates based on global nitrogen fluxes (*7*, *9*). Although denitrification induces A_T generation with the pore water, most of this is offset by water column nitrification and N_2 fixation, which consume A_T. Hence, the global contribution of denitrification to the marine A_T budget is limited to the inflow of nitrate from land and is at most 1.5 Tequiv A_T year^{-1} (*9*). Pyrite burial in the coastal, shelf, and slope seafloor generates an additional 2.9 Tequiv A_T year^{-1} in our model, which agrees with previous estimates based on the global sulfide burial flux (2.4 to 5.5 Tequiv A_T year^{-1}) (*7*) (table S4).

Anthropogenic impact on seafloor alkalinity generation

We used our biogeochemical model to quantify the impact of anthropogenically induced sediment disturbances on A_T generation. To emulate the impact of mobile bottom-contact fishing, we first simulated resuspension of the surface layer of the sediment. Subsequently, we simulated the redeposition of the top sedimentary layer by homogenizing the solid-phase particles and exchanging the pore water with the overlying water. To account for the uncertainty in our model results, we first defined probability distributions for each of the critical disturbance parameters (Materials and Methods) and used the 0.25, 0.50, and 0.75 quantiles of these distributions to define a lower, median, and higher model estimate, respectively (results are hence reported as median [lower, higher]). We varied disturbance frequencies from 1 to 10 times per year, which covers the annual mobile bottom-contact fishing frequency range in coastal and shelf seas (*14*). The mobile bottom-contact fishing impacts were simulated for coastal and shelf sands, coastal mud, shelf mud, and slope sediments, which are the areas where mobile bottom-contact fishing occurs most regularly (*14*). The impact on A_T generation is largest in muddy coastal areas, where mobile bottom-contact fishing leads to a decrease of up to 1.5 mequiv A_T m^{-2} year^{-1} relative to the natural efflux, whereas the impact is two orders of magnitude lower in the shelf sediments (Fig. 2A). Overall, the effect of mobile bottom-contact fishing appears negligible for sand and slope sediments, with a simulated impact on A_T fluxes in these sediment types that are several orders of magnitude smaller than the simulated A_T loss in coastal and shelf muds (Fig. 2A). All A_T loss in the mobile bottom-contact fishing scenario is caused by sediment resuspension and subsequent reoxidation of pyrite. Note that the oxidation of pyrite will form iron oxides, which could eventually settle out of the water column and become buried again. When such deposition occurs in the right environment, this could again lead to formation of pyrite, which would generate A_T and thus balance the initial loss of A_T upon oxidation. This could hence reduce the overall A_T loss due to disturbance and limit the associated reduction in marine CO_2 uptake. However, the iron oxides need to be deposited in the right coastal environment (sustaining anoxic sulfate reduction), and moreover, there is marked difference in timescale between reoxidation and reprecipitation. Where the oxidation of pyrite occurs over timescales of days to weeks (*37*), the process of resettling, burial, and reformation of pyrite would take years or longer. Additionally, the iron oxide particles could be transported with the dominant currents off the shelf and into deeper waters (*38*), which hence would lead to permanent A_T loss from the surface ocean (which is the critical layer that is in contact with atmospheric CO_2).

To estimate the global impact of mobile bottom-contact fishing on sedimentary A_T production, we combined our model results with spatial data on the frequency and extent of sediment disturbances induced by mobile bottom-contact fishing (Fig. 2B) (*14*). Mobile bottom-contact fishing affects 5,500,000 km^2 of sediment per year and causes a global A_T loss of 130 [55, 220] Gequiv year^{-1}. The highest impact is seen in the Adriatic and North Sea regions, which are also the more frequently fished areas (Fig. 2B and table S5). Despite more frequent disturbance of the seafloor than in the North Sea, the predicted impact on the A_T generation is relatively low in the Irish Sea and the Iberian Margin, as less mobile bottom-contact fishing occurs in muddy coastal sediments in these regions (Fig. 2B and table S5). Our results thus indicate that a sizeable reduction in global A_T loss can be achieved by limiting mobile bottom-contact fishing in muddy coastal areas.

Dredging-related disturbances were simulated by resuspending and homogenizing the complete sediment column, as several meters of sediment are generally excavated during dredging operations (*39*). We simulated dredging events to occur with a frequency of 1 to 5 per year, and a time lag between sediment excavation and deposition of 0.1 to 10 days. The dredging experiment was only conducted for muddy coastal sediment, as most dredging occurs in these environments (*40*). In the dredging scenario, up to 2.1 mequiv A_T m^{-2} year^{-1} is lost (Fig. 2C). Most of the A_T loss is due to the inhibition of pyrite burial, and the remaining 3 to 20% of the A_T loss is caused by stimulation of carbonate precipitation, with the highest relative contribution from the highest disturbance frequencies and lowest resuspension times. The increased carbonate precipitation is driven by introducing overlying water, oversaturated with respect to carbonates, at depth in the sediment. While the

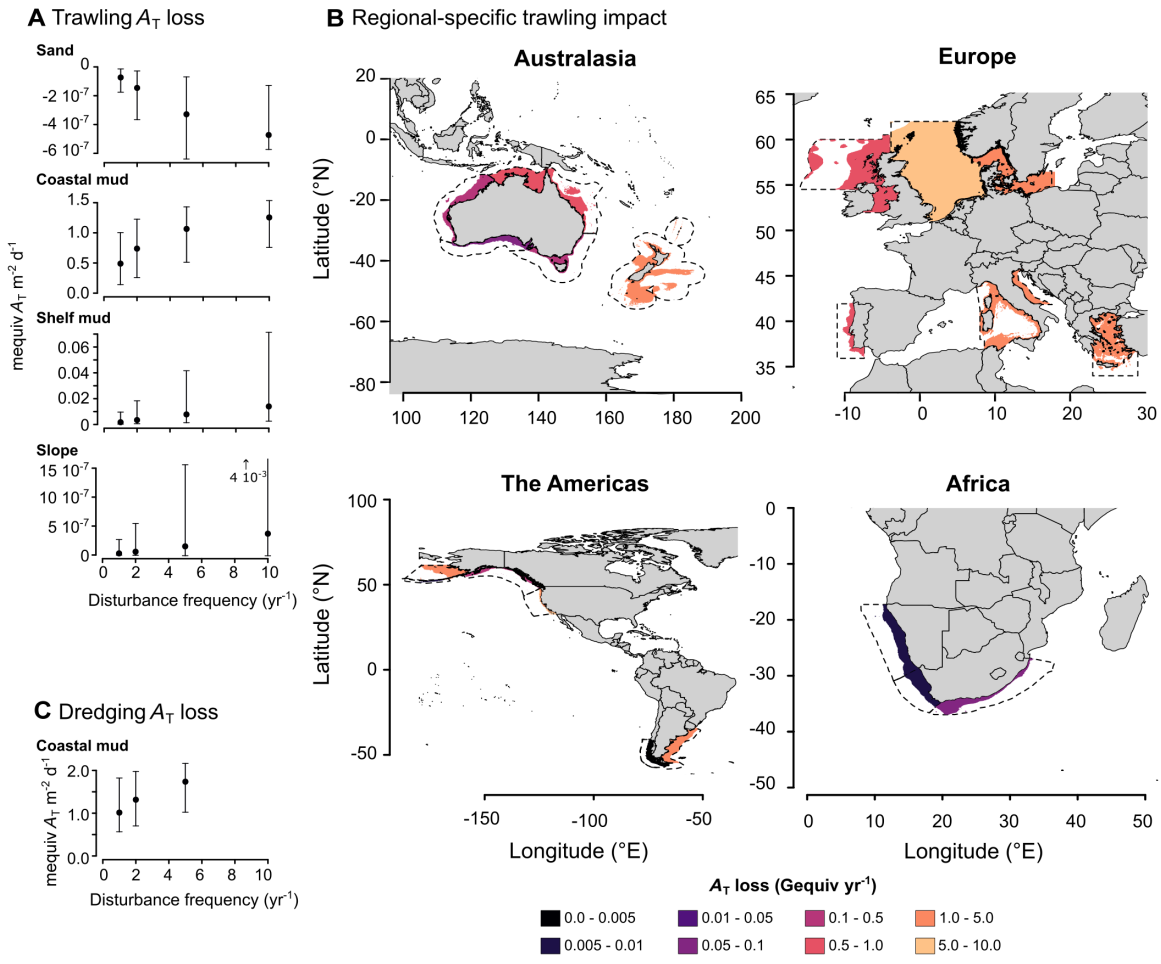

Fig. 2. Disturbance simulations. Loss of total alkalinity (A_T) due to sediment disturbances; negative values indicate A_T gain. (**A**) Impact of mobile bottom-contact fishing on different sediment types. Error bars indicate lower and higher impact simulations. Simulated pore-water profiles are shown in figs. S3 to S7. (**B**) Regional estimates of annual A_T loss due to mobile bottom-contact fishing in sediments <1000-m water depth. Areas delineated with dashed areas indicate the assessed region [based on (*14*)]. (**C**) Impact of dredging on muddy coastal sediments. Error bars indicate lower and higher impact simulations.

local effect of dredging on the sediment biogeochemistry is higher than for mobile bottom-contact fishing (Fig. 2, A and C), the smaller extent of dredged areas (~4000 km^2 year^{-1}) results in a 100-fold lower global A_T loss of 1.5 [0.8, 2.7] Gequiv year^{-1} as compared to mobile bottom-contact fishing.

Our results show that mobile bottom-contact fishing and dredging reduce the natural capacity of the seafloor to generate A_T. The global A_T loss due to mobile bottom-contact fishing and dredging amounts to 130 [56, 220] Gequiv year^{-1}. The amount of CO_2 that will be lost from the surface water due the loss of A_T can be estimated by the thermodynamic CO_2 buffer factor, which represents the change in the concentration of DIC upon the addition of 1 mol of A_T to the seawater, evaluated at a constant fugacity (or partial pressure) of CO_2 (*4*, *41*). This factor depends on the local seawater chemistry, temperature, and salinity, causing it to vary between different coastal systems (*7*). Across the global ocean, this factor can vary from 0.75 to 0.95, with an average value of 0.84 (*42*). Using the average, the A_T loss due to anthropogenic seafloor disturbances would lead to the transfer of 4.9 [2.1, 8.2] Tg CO_2 year^{-1} from the ocean to the atmosphere. This is comparable to the impact of mobile bottom-contact fishing on marine carbon sequestration via the inhibition of organic carbon burial, which is estimated to be 10 ± 30 Tg CO_2 year^{-1} (*27*, *28*). Anthropogenic sediment disturbances hence generate "hidden" indirect CO_2 emissions by affecting both inorganic and organic cycling, which are nevertheless small compared to the direct CO_2 emissions resulting from fossil fuel consumption (135 Tg CO_2 year^{-1}) of the global mobile bottom-contact fishing fleet (*43*). Still, these indirect emissions should not be ignored, particularly when compared to ongoing efforts to develop CDR capacity. Restoration of tens of millions of hectares of seagrass and mangrove ecosystems (*44*), at an estimated cost of 10^3 to 10^5 USD ha^{-1} (*45*), is expected to provide carbon sequestration in the range of 1 to 10 Tg CO_2 year^{-1} (*46*). Moreover, the current capacity for direct air capture of CO_2 is 0.04 Tg CO_2 year^{-1} and might reach 5 Tg CO_2 year^{-1} in 2030 provided that substantial investments take place (*47*, *48*). The A_T loss and resulting hidden CO_2 emissions caused by marine industries essentially offset gains currently made in CDR. Our results illustrate that the impact of mobile bottom-contact fishing and dredging on sedimentary A_T generation is non-negligible and thus should be considered when performing marine carbon accounting and making global carbon budgets. This potential important and

unrecognized A_T loss should inspire future research to experimentally validate the present model results.

MATERIALS AND METHODS

We aimed to simulate the impact of sediment disturbances by mobile bottom-contact fisheries and sediment dredging on natural alkalinity (A_T) generation. To this end, we constructed a sediment reaction-transport model that contains the essential biogeochemical reactions for A_T production: (i) denitrification, (ii) pyrite precipitation, and (iii) carbonate dissolution/precipitation. The organic matter mineralization part of the model is based on a previously published diagenetic model that can represent organic matter and nutrient cycling in sediments in settings that range from nearshore to the deep sea (*30*). We extended this model to explicitly account for pyrite precipitation, added an efficient pH calculation module (*31*), and included the most up-to-date formulation of carbonate precipitation and dissolution kinetics (*49*) (tables S1 and S2).

We used our sediment reaction-transport model first to simulate seafloor alkalinity generation in the four different habitats we defined based on our data compilation: coastal mud (<50 m water depth), shelf mud (<200 m water depth), slope (<2000 m water depth), and deep sea (>2000 m water depth). Because of the lack of metadata with respect to alkalinity-generating processes, we do not account for smaller-scale spatial variability, but rather focus on the first-order trends. All baseline parameters are taken from previous modeling studies, or global data compilations (table S3). Our model philosophy is that it is more informative to develop a simplified model that is suitably constrained by a large dataset than to use a complex model that cannot be constrained by data. Therefore, we used the combined alkalinity, DIC, and oxygen fluxes to validate the model, as complementary data needed to constrain alkalinity-generating processes, such as downcore profiles of pyrite and carbonate dissolution, were rare. This approach gives us a broader spatial coverage of data points and avoids the potential introduction of spatial bias toward specific environments.

We then used our baseline simulation for each of the four habitats and introduced sediment disturbance by resuspending the top sedimentary layer and homogenizing the sediment layer. Our assumptions and the assessment of model uncertainty are detailed below.

Diagenetic model formulation

The early diagenetic model follows the standard approach to describe reaction transport in marine sediments (*30*, *50*–*54*). The core of this reaction-transport model consists of a set of mass balance equations of the advection-diffusion-reaction form (*52*, *55*). Adopting the assumption of steady-state compaction, the balance equation for a pore-water solute and solid components becomes (*55*)

$$\varphi\frac{\partial C_{\mathrm{D},i}}{\partial t}=\frac{\partial}{\partial z}\left[\varphi D_{\mathrm{i}}\frac{\partial C_{\mathrm{D,i}}}{\partial z}-\varphi\nu_{\mathrm{F}}C_{\mathrm{D,i}}\right]+\varphi\alpha_{\mathrm{i}}(z)\left(C_{\mathrm{D,i}}^{\mathrm{OW}}-C_{\mathrm{D,i}}\right)+\sum_k\nu_{i,k}R_k \quad (1)$$

$$(1-\varphi)\frac{\partial C_{\mathrm{S,i}}}{\partial t}=\frac{\partial}{\partial z}\left[(1-\varphi)D_{\mathrm{b}}(z)\frac{\partial C_{\mathrm{S,i}}}{\partial z}-(1-\varphi)\nu_{\mathrm{S}}C_{\mathrm{S,i}}\right]+\sum_k\nu_{i,k}R_k$$

The quantity $C_{\mathrm{D,i}}$ represents the concentration of a pore-water compound, $C_{\mathrm{D,i}}^{\mathrm{OW}}$ is the value in the overlying water, φ denotes the porosity (assumed constant with depth), D_{i} is the diffusion coefficient, ν_{F} is the burial velocity of the pore fluids, ν_{S} is the burial velocity of the solids, and z is the depth into the sediment. The concentration of a solid compound $C_{\mathrm{S,i}}$ is expressed per unit volume of solid sediment. The quantities R_k represent the rates of the biogeochemical reactions (expressed per bulk sediment volume), where $\nu_{i,k}$ is the stoichiometric coefficient of the ith species in the kth reaction. The effect of bioturbation (bio-mixing and bio-irrigation) is implemented by the bio-mixing parameter D_{b} and the bio-irrigation parameter α_{i}, which is solute specific (*56*).

Model parameterization: Transport processes

The model includes a set of transport processes that is characteristic for sediments affected by fauna: (i) solute diffusion in the pore water, (ii) downward advection due to sediment accumulation, (iii) bio-mixing, and (iv) bio-irrigation. Pore-water advection induced by bottom currents and waves in the sandy (permeable) simulation is incorporated by increasing and deepening bio-irrigation.

The solute flux due to molecular diffusion and advection is described by Fick's first law (*57*)

$$J_{\mathrm{D}}=-\varphi D_{\mathrm{i}}\frac{\partial C_{\mathrm{D,i}}}{\partial z}+\varphi\nu_{\mathrm{F}}C_{\mathrm{D,i}} \quad (2)$$

where D_{i} is calculated by first determining the molecular diffusion coefficient $D_{\mathrm{i}}^{\mathrm{mol}}$ as a function of temperature and salinity using the CRAN:marelac package (*58*) and corrected for tortuosity according to the modified Weissberg relation (*59*)

$$D_{\mathrm{i}}=\frac{D_{\mathrm{i}}^{\mathrm{mol}}}{1-2\ln\varphi} \quad (3)$$

The presence of bioturbation is modeled as two different extra transport parameters: bio-mixing and bio-irrigation. Following the conventional description, bio-mixing is modeled as a diffusive-like process (*52*, *60*)

$$J_{\mathrm{B}}=-(1-\varphi)D_{\mathrm{B}}\frac{\partial C_{\mathrm{S,i}}}{\partial z} \quad (4)$$

Benthic fauna requires food resources (organic matter) that arrive from the overlying water at the top of the sediment pile, and thus, most of their activity occurs near the sediment-water interface and decreases with sediment depth (*61*). The bio-diffusivity coefficient accordingly follows a sigmoidal depth profile (*62*)

$$D_{\mathrm{b}}(z)=D_{\mathrm{b,0}}\exp\left[-\frac{(z-z_{\mathrm{L}})}{0.25z_{\mathrm{bm,att}}}\Big/\left(1+\frac{(z-z_{\mathrm{L}})}{0.25z_{\mathrm{bm,att}}}\right)\right] \quad (5)$$

where $D_{\mathrm{b,0}}$ is the bio-diffusivity at the sediment-water interface, z_{L} is the depth of the mixed layer, and $z_{\mathrm{bm,att}}$ is an attenuation coefficient determining the transition zone from mixed to unmixed sediment horizons. Bio-mixing is governed by two separate parameters: the intensity of mixing as represented by the bio-diffusivity, $D_{\mathrm{b,0}}$, and the depth of the mixed layer, as represented by z_{L} (the width of the transition zone $z_{\mathrm{bm,att}}$ is of secondary importance). In natural systems, these two parameters are correlated (*62*, *63*). Hence, to account for this interdependency, and facilitate model sensitivity analysis, the mixing depth was made dependent on the bio-diffusivity using the following relation

$$z_L=z_{L,0}+z_{L,\max}\left(1-e^{-D_{\mathrm{b,0}}/D_{\mathrm{b,ref}}}\right) \quad (6)$$

where $L_{z,0}$ (= 1 cm) is the minimum depth of bioturbation, $L_{z,\max}$ is the maximum mixing depth [$L_{z,0}+L_{z,\max}$ = 10 cm; (*62*)], and $D_{\mathrm{b,ref}}$ (= 3 $\mathrm{cm^2\ year^{-1}}$) is a reference mixing intensity (*53*). This relation

implies that the mixing depth initially rapidly increases with a rising mixing intensity, but then saturates. This saturation response implies that when the mixing intensity of the infauna increases, the burrowing depth does not necessarily increase.

The second effect of bioturbating fauna, bio-irrigation, is typically described as a nonlocal exchange process, in which pore-water parcels are exchanged with bottom water parcels (*64*, *65*)

$$I_{irr}(z) = \alpha_i(z)\left(C_{D,i}^{OW} - C_{D,i}\right) \quad (7)$$

where the quantity $\alpha_i(z)$ represents the depth-dependent irrigation intensity, $C_{D,i}{}^{ow}$ is the solute concentration of the bottom water, and $C_{D,i}$ is the solute concentration at depth z. The bio-irrigation effect is generally most pronounced in the top layer of the sediment. However, the faunal activities that induce bio-mixing (e.g., locomotion and burrow construction) are different from those that drive bio-irrigation (e.g., burrow ventilation), and so the depth dependency of both processes does not need to be the same. Indeed, in natural systems, bio-irrigation is best represented using an exponential relationship (*66*) of the form

$$\alpha_i(z) = \alpha_{i,0} e^{-z/z_{irr,att}} \quad (8)$$

where $\alpha_{i,0}$ is the bio-irrigation coefficient at the sediment-water interface and $z_{irr,att}$ is an attenuation coefficient determining the transition zone from irrigated to un-irrigated sediment horizons. Following (*56*), we introduce solute-specific irrigation coefficients to capture the differential biogeochemical behavior of individual pore-water species.

Model parameterization: Reaction processes

Total alkalinity is treated as a conservative species and is transported identically to other dissolved species. All reactions in table S1 are written in terms of A_T-neutral species, except for the protons (H^+). As such, each of the reactions in table S2 can produce or consume A_T. The pH is then calculated at each time step from A_T and DIC ($\sum CO_2$) using the SolveSAPHE subroutine of (*31*). Because A_T is treated as a conservative species, all acid-base species are modeled as total dissolved components.

The focus of the reaction-transport model was to simulate A_T generation within marine sediments. Therefore, we tailored the reaction set to the most important processes generating A_T: (i) carbonate dissolution/precipitation, (ii) pyrite formation, and (iii) denitrification (*6*, *7*, *9*). To keep the reaction set as simple as possible, we did not explicitly model iron oxides, but instead allowed pyrite to precipitate during sulfate reduction, following (*30*). The reactions included in the model are listed in table S1, the reaction equations are listed in table S2, and the parameters and boundary conditions are given in table S3.

Table S1 specifies the 12 reactions that are included in the reaction list. The model describes organic matter degradation kinetics by a three-component multi-*G* model (*67*, *68*). Each of the organic matter ("*G*") fractions can be degraded by four different mineralization pathways: aerobic respiration, denitrification, sulfate reduction, and methanogenesis. Note that these redox pathways are implemented for each of the organic matter fractions. The redox sequence is implemented via conventional limitation-inhibition formulations (table S2) (*30*, *50*, *68*). Organic matter mineralization produces DIC ($\sum CO_2$), ammonium ($\sum NH_4^+$), and phosphate ($\sum H_2PO_4^-$). Ammonium can be oxidized with oxygen during nitrification. Denitrification produces N_2 gas, which is considered inert and escapes the sediment via diffusion and irrigation. During sulfate ($\sum SO_4^{2-}$) reduction, a fraction of the reduced sulfide ($\sum H_2S$) is assumed to immediately precipitate as pyrite (FeS_2) [comparable to the approach taken in (*30*)], whereas the rest can be re-oxidized by oxygen or nitrate ($\sum NO_3^-$). When other electron acceptors (O_2, $\sum NO_3^-$, $\sum SO_4^{2-}$) are depleted, methanogenesis produces methane (CH_4), which can be oxidized by oxygen or sulfate. The kinetic rate expressions of all re-oxidation processes are described by standard second-order rate laws (table S2).

Two polymorphs of carbonate minerals are included: low-magnesium calcite ($CaCO_3{}^{calcite}$) and aragonite ($CaCO_3{}^{aragonite}$), both of which settle on the sediment at fixed rates (table S3). When these minerals become undersaturated, they are allowed to dissolve. When the pore water becomes oversaturated with respect to calcite, calcite is allowed to precipitate (table S2).

Disturbance simulation

For the mobile bottom-contact fishing disturbance, we estimated the amount of sediment eroded (m_{ero}) based on the silt fraction and hydrodynamic drag created by a passing trawl (*69*–*71*), assuming a silt fraction (s_f, unitless) of 0.5 for muddy sediments and 0.1 for sandy sediments, and a hydrodynamic drag (D_H, in N m^{-1}) of a large beam trawling vessel [see (*69*) for details]

$$m_{ero} = 2.602 * s_f + 1.206\ 10^{-3} D_H + 1.321\ 10^{-2}\ s_f D_H \quad (9)$$

The erosion depth was then calculated from the eroded mass, porosity, and solid-phase density $\left[d_{ero} = \frac{m_{ero}}{(\varphi + \rho_{solid}\varphi)}\right]$. We then allowed the eroded sediment to react in oxygenated water while it is resuspended. After reaction, we homogenized the solid-phase particles in the sediment column down to the penetration depth, and we set the pore-water concentrations down to that depth to the value of the overlying water. This is the same procedure as in previous transient disturbance modeling studies (*17*). We then transiently simulated the evolution of diagenetic processes. We allowed 1, 2, 5, and 10 disturbance events per year, which were distributed evenly throughout the year. We simulated 50 years for the sandy sediment experiment, 60 years for the coastal and shelf muddy experiment, and 150 years for the slope experiment. These time frames were chosen to allow the sediment to reach a new steady state.

The dredging experiment was only simulated for the coastal muddy site because dredging occurs mainly in these types of environments. In the dredging case, we eroded and homogenized the complete sediment column (20 cm) and allowed it to react in oxygenated conditions for 0.1, 1, and 10 days to simulate the varying time between dredging and redeposition. We simulated 1, 2, and 5 dredging events per year, although the most common occurrence is maintenance dredging, which generally occurs once per year. The rest of the simulation was identical to the mobile bottom-contact fishing experiments.

Uncertainty estimation

To account for the uncertainty in our model results, we have defined a plausible parameter distribution for the critical disturbance parameters (log-normal for resuspension time, gaussian for erosion depth and penetration depth) (Fig. 3). We used the 0.25, 0.50, and 075 quantile of each parameter to define our lower, median, and upper bound estimates, respectively. The probability distribution of resuspension time was calculated from the height distribution of particles within a resuspended plume after a passing trawl [between 0 and 6 m, with a mean of ~1 m (*72*)] and the observed settling velocity of resuspended particles under natural conditions in m day^{-1}, which follows

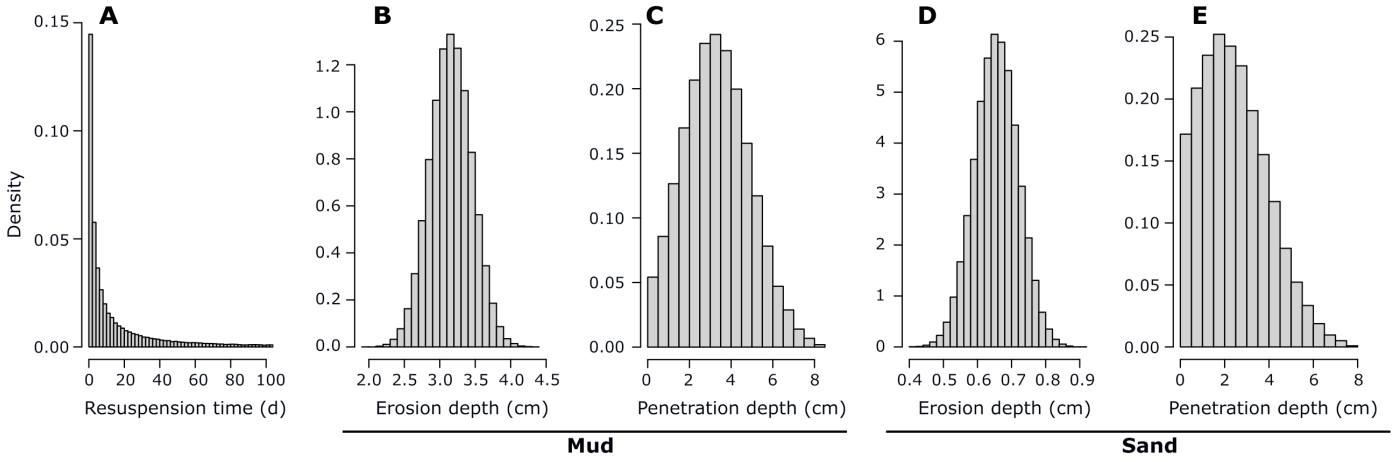

Fig. 3. Disturbance parameter probability distributions. (**A**) Time a particle stays in solution after resuspension (quantiles: 0.25 = 1.5 days, 0.50 = 6.8 days, 0.75 = 30 days). (**B**) Erosion depth of muddy sediment (quantiles: 0.25 = 3.0 cm, 0.50 = 3.2 cm, 0.75 = 3.4 cm). (**C**) Gear penetration depth in muddy sediment (quantiles: 0.25 = 2.2 cm, 0.50 = 3.3 cm, 0.75 = 4.4 cm). (**D**) Erosion depth of sandy sediment (quantiles: 0.25 = 0.61 cm, 0.50 = 0.65 cm, 0.75 = 0.70 cm). (**E**) Gear penetration depth in sandy sediment (quantiles: 0.25 = 1.3 cm, 0.50 = 2.3 cm, 0.75 = 3.4 cm).

a logarithmic distribution with a mean and SD on the log scale of −2 and 2, respectively (*73*). The probability distribution for erosion depth in mud and sand was calculated from Eq. 9, using a silt fraction of 0.5 for muddy sediments and 0.1 for sandy sediments, and the uncertainty on D_H was given in (*69*), which gives us an erosion depth between 2 and 4 cm, and agrees well with before-after experimental studies (*74*, *75*). The probability distribution for penetration depths was taken from the beam trawl data from (*76*).

Data for dredging impacts are less readily available. To account for the uncertainty, we used 0.1, 1, and 10 days of resuspension as lower, median, and upper bound estimates.

Numerical model solution

The numerical solution procedure has been described in detail previously (*17*, *53*, *54*). In brief, the open-source programming language R (*77*) was used to implement a numerical solution procedure for the partial differential equations by applying the method-of-lines (*78*) using the R packages CRAN:ReacTran (*79*) and CRAN:deSolve (*80*). The sediment grid was generated by dividing the sediment domain into an uneven grid of 200 layers, with the thickness of the first layer being 0.01 cm and the thickness of the other layers increasing with a factor of 1.018. The steady state of the baseline simulations was calculated by integrating the resulting set of ordinary differential equations using the steady state solver routine "lsode" within the package CRAN:deSolve. The transient scenario simulations were integrated using the stiff equation solver routine "vode" (*81*) within the package CRAN:deSolve.

Global estimates

To make a map of global seafloor A_T release, we retrieved a map of seabed substrate from (*82*) and combined this with an ocean bathymetry grid retrieved from (*83*). When the substrate was gravel, we assumed no A_T flux. When the substrate was sand, we assumed that the A_T flux was constant and equal to 4.9 mequiv A_T m^{-2} day^{-1} (our model-derived flux from sandy sediments). When the substrate was mud, we calculated the A_T flux from the bathymetry using the relation between seafloor A_T flux and water depth (WD) for muddy sediments derived from our model simulations (Fig. 4)

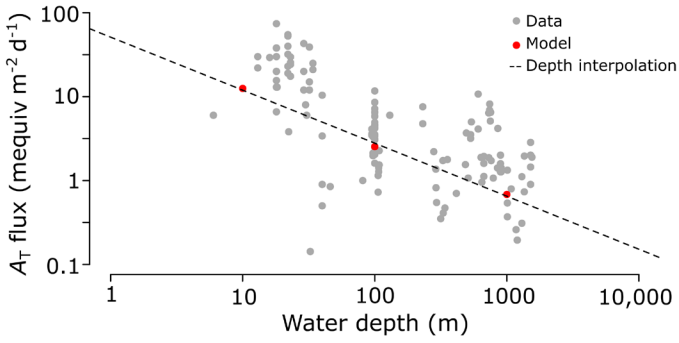

Fig. 4. Depth interpolation to derive a spatial map of seafloor alkalinity release. The depth interpolation is based on the modeled fluxes and shows good agreement with the data.

$$F_{A_T} = 10^{-0.6319\log_{10}(\mathrm{WD})+1.7093} \quad (10)$$

To make an estimate of the global impact of mobile bottom-contact fishing on seafloor A_T generation, we use the modeled relation between disturbance frequency [equivalent to the swept area ratio (SAR)] and A_T loss per surface area (in mequiv m^{-2} day^{-1}) for our lower, median, and upper bound model results. Because denitrification did not lead to a net A_T gain, we only considered the impact on carbonate dissolution and pyrite precipitation. We subsequently combine this relationship with the database on global mobile bottom-contact fishing intensity collected by (*14*). This dataset divides fishing intensity into two depth regions (<200 m and 200 to 1000 m) and gives the areal coverage of sand, mud, and gravel, as well as the SAR for each grid cell. We assumed that the fishing intensity at <200 m was equally distributed between coastal and shelf settings [based on the findings for the North Sea (*84*)]. Subsequently, we calculated the total A_T loss per region by converting SAR to A_T loss per surface area by interpolating our modeled results and subsequently multiplying with the trawled area of the grid cell. Because the dataset of (*14*) only contains about 20% of all global trawled areas, we multiplied our total

A_T loss by 5 to arrive at a global estimate of A_T loss due to mobile bottom-contact fishing.

Global sediment volumes dredged annually are not reported. We used the dredging volumes of the OSPAR Maritime Area (which includes Belgium, Denmark, France, Germany, Iceland, Ireland, The Netherlands, Norway, Portugal, Spain, Sweden, and the UK) in 2021 ($M_{\text{dredged,EU}}$ ~280 million tons of dry sediment) (*40*). We can then estimate the seabed surface that is dredged annually as

$$A_{\text{dredged,EU}} = \frac{M_{\text{dredged,EU}}}{(1-\varphi)\rho_{\text{sed}}} / h_{\text{dredged}} \quad (11)$$

where ρ_{sed} is the density of dry sediment (2600 kg m^{-3}), φ is the porosity (0.8 for muddy sediments), and h_{dredged} is the height of the sedimentary layer that is dredged. While values for h_{dredged} are also not readily available, this is typically between 0.5 and 2 m (*39*), so we here assume that h_{dredged} is ~1 m. This gives us a dredged surface area of ~540 million m^2 in the OSPAR Maritime Area. To upscale the value of the EU to a global value, we calculated the fraction of the Exclusive Economic Zone (EEZ) of the countries included in the OSPAR Maritime Area relative to the global EEZ surface. Because dredging mostly occurs to maintain navigation channels and in harbors, we only considered the part of the EEZ that is on the continental shelf. The OSPAR Maritime Area represents 13% of the total continental shelf EEZ surface, so our estimated seabed surface dredged globally is

$$A_{\text{dredged,global}} = A_{\text{dredged,EU}} / 0.13 \quad (12)$$

The global seabed surface that is dredged annually then becomes 4000 km^2, and the global dredged mass is 2.1 billion tons of dry sediment.

Model limitations

The aim of our model was to quantify the global alkalinity destruction caused by anthropogenic sediment disturbances, and in the model development, several assumptions were made that need consideration. Foremost, the model has no explicit spatial component, and hence, we assumed that all mobile bottom-contact fishing and dredging disturbances are similar across each defined habitat. In reality, mobile bottom-contact fishing and dredging intensity and impacts are spatially variable, and part of the resuspended material will be transported by currents and will settle elsewhere or transported offshore (*28*, *38*). Additionally, to be able to estimate the global anthropogenic impact, we upscaled from the regions for which we did have data (the ICES dataset for mobile-contact bottom fishing and the OSPAR maritime area for dredging). To make this upscaling, we had to assume that the fishing effort in the remaining 80% of fishing grounds is comparable to that of the documented 20%, and that the dredging activity in the documented 13% of the global EEZ is also representative for the remaining 87%. Because of the lack of a spatial component and the need for extrapolation, our results should not be used to inform local policymaking, but rather as a guide to investigate the impact of dredging and mobile bottom-contact fishing on regional and global scales. Additionally, there are currently no experimental data available that could be used to validate our model results. For example, we assumed that benthic faunal communities always recovered to their initial bio-mixing and bio-irrigation intensities, which is not necessarily the case. Therefore, our model result should be seen as a first-order estimate, and future research should conduct targeted experiments to verify the model projections.

Supplementary Materials

The PDF file includes:

Figs. S1 to S7
Tables S1 to S5
Legend for data S1
References

Other Supplementary Material for this manuscript includes the following:

Data S1

REFERENCES AND NOTES

1. J. Terhaar, T. L. Frölicher, F. Joos, Observation-constrained estimates of the global ocean carbon sink from Earth system models. *Biogeosciences* **19**, 4431–4457 (2022).
2. G. R. Bigg, T. D. Jickells, P. S. Liss, T. J. Osborn, The role of the oceans in climate. *Int. J. Climatol.* **23**, 1127–1159 (2003).
3. P. Friedlingstein, M. O'Sullivan, M. W. Jones, R. M. Andrew, D. C. E. Bakker, J. Hauck, P. Landschützer, C. Le Quéré, I. T. Luijkx, G. P. Peters, W. Peters, J. Pongratz, C. Schwingshackl, S. Sitch, J. G. Canadell, P. Ciais, R. B. Jackson, S. R. Alin, P. Anthoni, L. Barbero, N. R. Bates, M. Becker, N. Bellouin, B. Decharme, L. Bopp, I. B. M. Brasika, P. Cadule, M. A. Chamberlain, N. Chandra, T.-T.-T. Chau, F. Chevallier, L. P. Chini, M. Cronin, X. Dou, K. Enyo, W. Evans, S. Falk, R. A. Feely, L. Feng, D. J. Ford, T. Gasser, J. Ghattas, T. Gkritzalis, G. Grassi, L. Gregor, N. Gruber, Ö. Gürses, I. Harris, M. Hefner, J. Heinke, R. A. Houghton, G. C. Hurtt, Y. Iida, T. Ilyina, A. R. Jacobson, A. Jain, T. Jarníková, A. Jersild, F. Jiang, Z. Jin, F. Joos, E. Kato, R. F. Keeling, D. Kennedy, K. K. Goldewijk, J. Knauer, J. I. Korsbakken, A. Körtzinger, X. Lan, N. Lefèvre, H. Li, J. Liu, Z. Liu, L. Ma, G. Marland, N. Mayot, P. C. McGuire, G. A. McKinley, G. Meyer, E. J. Morgan, D. R. Munro, S.-I. Nakaoka, Y. Niwa, K. M. O'Brien, A. Olsen, A. M. Omar, T. Ono, M. Paulsen, D. Pierrot, K. Pocock, B. Poulter, C. M. Powis, G. Rehder, L. Resplandy, E. Robertson, C. Rödenbeck, T. M. Rosan, J. Schwinger, R. Séférian, T. L. Smallman, S. M. Smith, R. Sospedra-Alfonso, Q. Sun, A. J. Sutton, C. Sweeney, S. Takao, P. P. Tans, H. Tian, B. Tilbrook, H. Tsujino, F. Tubiello, G. R. van der Werf, E. van Ooijen, R. Wanninkhof, M. Watanabe, C. Wimart-Rousseau, D. Yang, X. Yang, W. Yuan, X. Yue, S. Zaehle, J. Zeng, B. Zheng, Global Carbon Budget 2023. *Earth Syst. Sci. Data.* **15**, 5301–5369 (2023).
4. R. E. Zeebe, D. Wolf-Gladrow, *CO_2 in Seawater: Equilibrium, Kinetics, Isotopes* (Gulf Professional Publishing. 2001).
5. National Academies of Sciences, Engineering, and Medicine. *A Research Strategy for Ocean-Based Carbon Dioxide Removal and Sequestration* (National Academies Press, 2022).
6. V. Krumins, M. Gehlen, S. Arndt, P. Van Cappellen, P. Regnier, Dissolved inorganic carbon and alkalinity fluxes from coastal marine sediments: Model estimates for different shelf environments and sensitivity to global change. *Biogeosciences* **10**, 371–398 (2013).
7. J. J. Middelburg, K. Soetaert, M. Hagens, Ocean alkalinity, buffering and biogeochemical processes. *Rev. Geophys.* **58**, e2019RG000681 (2020).
8. G. Müller, J. Börker, A. Sluijs, J. J. Middelburg, Detrital carbonate minerals in Earth's element cycles. *Global Biogeochem. Cycles* **36**, e2021GB007231 (2022).
9. X. Hu, W.-J. Cai, An assessment of ocean margin anaerobic processes on oceanic alkalinity budget. *Global Biogeochem. Cycles* **25**, (2011).
10. J. D. Milliman, A. W. Droxler, Neritic and pelagic carbonate sedimentation in the marine environment: Ignorance is not bliss. *Geol. Rundsch.* **85**, 496–504 (1996).
11. A. M. F. Rao, S. Y. Malkin, F. Montserrat, F. J. R. Meysman, Alkalinity production in intertidal sands intensified by lugworm bioirrigation. *Estuar. Coast. Shelf Sci.* **148**, 36–47 (2014).
12. Burdige, D. J. *Geochemistry of Marine Sediments* (Princeton Univ. Press, 2006).
13. B. S. Halpern, M. Frazier, J. Afflerbach, J. S. Lowndes, F. Micheli, C. O'Hara, C. Scarborough, K. A. Selkoe, Recent pace of change in human impact on the world's ocean. *Sci. Rep.* **9**, 11609 (2019).
14. R. O. Amoroso, C. R. Pitcher, A. D. Rijnsdorp, R. A. McConnaughey, A. M. Parma, P. Suuronen, O. R. Eigaard, F. Bastardie, N. T. Hintzen, F. Althaus, S. J. Baird, J. Black, L. Buhl-Mortensen, A. B. Campbell, R. Catarino, J. Collie, J. H. Cowan, D. Durholtz, N. Engstrom, T. P. Fairweather, H. O. Fock, R. Ford, P. A. Gálvez, H. Gerritsen, M. E. Góngora, J. A. González, J. G. Hiddink, K. M. Hughes, S. S. Intelmann, C. Jenkins, P. Jonsson, P. Kainge, M. Kangas, J. N. Kathena, S. Kavadas, R. W. Leslie, S. G. Lewis, M. Lundy, D. Makin, J. Martin, T. Mazor, G. Gonzalez-Mirelis, S. J. Newman, N. Papadopoulou, P. E. Posen, W. Rochester, T. Russo, A. Sala, J. M. Semmens, C. Silva, A. Tsolos, B. Vanelslander, C. B. Wakefield, B. A. Wood, R. Hilborn, M. J. Kaiser, S. Jennings, Bottom trawl fishing footprints on the world's continental shelves. *Proc. Natl. Acad. Sci. U.S.A.* **115**, E10275–E10282 (2018).
15. D. A. Kroodsma, J. Mayorga, T. Hochberg, N. A. Miller, K. Boerder, F. Ferretti, A. Wilson, B. Bergman, T. D. White, B. A. Block, P. Woods, B. Sullivan, C. Costello, B. Worm, Tracking the global footprint of fisheries. *Science* **359**, 904–908 (2018).
16. F. K. J. Oberle, C. D. Storlazzi, T. J. J. Hanebuth, What a drag: Quantifying the global impact of chronic bottom trawling on continental shelf sediment. *J. Mar. Syst.* **159**, 109–119 (2016).

17. S. J. van de Velde, V. Van Lancker, S. Hidalgo-Martinez, W. M. Berelson, F. J. R. Meysman, Anthropogenic disturbance keeps the coastal seafloor biogeochemistry in a transient state. *Sci. Rep.* **8**, 1–10 (2018).
18. J. C. Tiano, R. Witbaard, M. J. N. Bergman, P. van Rijswijk, A. Tramper, D. van Oevelen, K. Soetaert, Acute impacts of bottom trawl gears on benthic metabolism and nutrient cycling. *ICES J. Mar. Sci.* **76**, 1917–1930 (2019).
19. J. D. Rimstidt, D. J. Vaughan, Pyrite oxidation: A state-of-the-art assessment of the reaction mechanism. *Geochim. Cosmochim. Acta* **67**, 873–880 (2003).
20. E. De Borger, J. Tiano, U. Braeckman, A. Rijnsdorp, K. Soetaert, Impact of bottom trawling on sediment biogeochemistry: A modelling approach. *Biogeosciences* **18**, 1–32 (2020).
21. C. L. Hurd, C. S. Law, L. T. Bach, D. Britton, M. Hovenden, E. R. Paine, J. A. Raven, V. Tamsitt, P. W. Boyd, Forensic carbon accounting: Assessing the role of seaweeds for carbon sequestration. *J. Phycol.* **58**, 347–363 (2022).
22. J. R. Krause, A. Hinojosa-Corona, A. B. Gray, J. C. Herguera, J. McDonnell, M. V. Schaefer, S. C. Ying, E. B. Watson, Beyond habitat boundaries: Organic matter cycling requires a system-wide approach for accurate blue carbon accounting. *Limnol. Oceanogr.* **67**, S6–S18 (2022).
23. T. B. Atwood, A. Romanou, T. DeVries, P. E. Lerner, J. S. Mayorga, D. Bradley, R. B. Cabral, G. A. Schmidt, E. Sala, Atmospheric CO_2 emissions and ocean acidification from bottom-trawling. *Front. Mar. Sci.* **10**, 1125137 (2024).
24. E. Sala, J. Mayorga, D. Bradley, R. B. Cabral, T. B. Atwood, A. Auber, W. Cheung, C. Costello, F. Ferretti, A. M. Friedlander, S. D. Gaines, C. Garilao, W. Goodell, B. S. Halpern, A. Hinson, K. Kaschner, K. Kesner-Reyes, F. Leprieur, J. McGowan, L. E. Morgan, D. Mouillot, J. Palacios-Abrantes, H. P. Possingham, K. D. Rechberger, B. Worm, J. Lubchenco, Protecting the global ocean for biodiversity, food and climate. *Nature* **592**, 397–402 (2021).
25. G. Epstein, J. J. Middelburg, J. P. Hawkins, C. R. Norris, C. M. Roberts, The impact of mobile demersal fishing on carbon storage in seabed sediments. *Glob. Chang. Biol.* **28**, 2875–2894 (2022).
26. J. G. Hiddink, S. J. Van De Velde, R. A. McConnaughey, E. De Borger, J. Tiano, M. J. Kaiser, A. Sweetman, M. Sciberras, Quantifying the carbon benefits of ending bottom trawling. *Nature* **617**, E1–E2 (2023).
27. L. Porz, W. Zhang, N. Christiansen, J. Kossack, U. Daewel, C. Schrum, Quantification and mitigation of bottom-trawling impacts on sedimentary organic carbon stocks in the North Sea. *Biogeosciences* **21**, 2547–2570 (2024).
28. W. Zhang, L. Porz, R. Yilmaz, K. Wallmann, T. Spiegel, A. Neumann, M. Holtappels, S. Kasten, J. Kuhlmann, N. Ziebarth, B. Taylor, H. T. M. Ho-Hagemann, F.-D. Bockelmann, U. Daewel, L. Bernhardt, C. Schrum, Long-term carbon storage in shelf sea sediments reduced by intensive bottom trawling. *Nat. Geosci.* **17**, 1268–1276 (2024).
29. J. Tiano, E. De Borger, S. Paradis, C. Bradshaw, C. Morys, A. Pusceddu, C. Ennas, K. Soetaert, P. Puig, P. Masqué, M. Sciberras, Global meta-analysis of demersal fishing impacts on organic carbon and associated biogeochemistry. *Fish Fish.* **25**, 936–950 (2024).
30. K. Soetaert, P. M. J. Herman, J. J. Middelburg, A model of early diagenetic processes from the shelf To abyssal depths. *Geochim. Cosmochim. Acta* **60**, 1019–1040 (1996).
31. G. Munhoven, Mathematics of the total alkalinity–pH equation—Pathway to robust and universal solution algorithms: The SolveSAPHE package v1.0.1. *Geosci. Model Dev.* **6**, 1367–1388 (2013).
32. J. P. Dunne, J. L. Sarmiento, A. Gnanadesikan, A synthesis of global particle export from the surface ocean and cycling through the ocean interior and on the seafloor. *Global Biogeochem. Cycles* **21**, 1–16 (2007).
33. J. J. Middelburg, K. Soetaert, P. M. J. Herman, Empirical relationships for use in global diagenetic models. *Deep-Sea Res. I* **44**, 327–344 (1997).
34. B. S. Halpern, S. Walbridge, K. A. Selkoe, C. V. Kappel, F. Micheli, C. D'Agrosa, J. F. Bruno, K. S. Casey, C. Ebert, H. E. Fox, R. Fujita, D. Heinemann, H. S. Lenihan, E. M. P. Madin, M. T. Perry, E. R. Selig, M. Spalding, R. Steneck, R. Watson, A global map of human impact on marine ecosystems. *Science* **319**, 948–952 (2008).
35. R. C. Aller, Carbonate dissolution in nearshore terrigenous muds: The role of physical and biological reworking. *J. Geol.* **90**, 79–95 (1982).
36. M. A. Green, R. C. Aller, Early diagenesis of calcium carbonate in Long Island Sound sediments: Benthic fluxes of Ca^{2+} and minor elements during seasonal periods of net dissolution. *J. Mar. Res.* **59**, 769–794 (2001).
37. J. W. Morse, Oxidation kinetics of sedimentary pyrite in seawater. *Geochim. Cosmochim. Acta* **55**, 3665–3667 (1991).
38. S. Paradis, P. Puig, A. Sanchez-Vidal, P. Masqué, J. Garcia-Orellana, A. Calafat, M. Canals, Spatial distribution of sedimentation-rate increases in Blanes Canyon caused by technification of bottom trawling fleet. *Prog. Oceanogr.* **169**, 241–252 (2018).
39. ABPmer. Maintenance Dredging BPEO (R2919) (2018). https://marine.gov.scot/sites/default/files/bpeo_1.pdf.
40. ODIMS—Submission: OSPAR Dumping and Placement of Wastes or Other Matter at Sea 2021. https://odims.ospar.org/en/submissions/ospar_dumping_at_sea_2021_01/.
41. L. J. J. Geerts, A. Hylén, F. J. R. Meysman, Review and syntheses: Ocean alkalinity enhancement and carbon dioxide removal through marine enhanced rock weathering using olivine. *Biogeosciences* **22**, 355–384 (2025).
42. M. Frankignoulle, A complete set of buffer factors for acid/base CO2 system in seawater. *J. Mar. Syst.* **5**, 111–118 (1994).
43. R. W. R. Parker, J. L. Blanchard, C. Gardner, B. S. Green, K. Hartmann, P. H. Tyedmers, R. A. Watson, Fuel use and greenhouse gas emissions of world fisheries. *Nat Clim Change* **8**, 333–337 (2018).
44. P. I. Macreadie, M. D. P. Costa, T. B. Atwood, D. A. Friess, J. J. Kelleway, H. Kennedy, C. E. Lovelock, O. Serrano, C. M. Duarte, Blue carbon as a natural climate solution. *Nat. Rev. Earth Environ.* **2**, 826–839 (2021).
45. J. Su, D. A. Friess, A. Gasparatos, A meta-analysis of the ecological and economic outcomes of mangrove restoration. *Nat. Commun.* **12**, 5050 (2021).
46. M. Fakhraee, N. J. Planavsky, C. T. Reinhard, Ocean alkalinity enhancement through restoration of blue carbon ecosystems. *Nat. Sustain.* **6**, 1–8 (2023).
47. M. Ozkan, S. P. Nayak, A. D. Ruiz, W. Jiang, Current status and pillars of direct air capture technologies. *iScience* **25**, 103990 (2022).
48. IEA. Direct Air Capture—Energy System. https://www.iea.org/energy-system/carbon-capture-utilisation-and-storage/direct-air-capture.
49. O. Sulpis, M. P. Humphreys, M. M. Wilhelmus, D. Carroll, W. M. Berelson, D. Menemenlis, J. J. Middelburg, J. F. Adkins, RADIv1: A non-steady-state early diagenetic model for ocean sediments in Julia and MATLAB/GNU Octave. *Geosci. Model Dev.* **15**, 2105–2131 (2022).
50. P. Berg, S. Rysgaard, B. Thamdrup, Dynamic modeling of early diagenesis and nutrient cycling. A case study in an Artic marine sediment. *Am. J. Sci.* **303**, 905–955 (2003).
51. Y. Wang, P. Van Cappellen, A multicomponent reactive transport model of early diagenesis: Application to redox cycling in coastal marine sediments. *Geochim. Cosmochim. Acta*, **60**, 2993–3014 (1996).
52. B. P. Boudreau, *Diagenetic Models and Their Implementation* (Springer-Verlag, 1997).
53. S. J. van de Velde, F. J. R. Meysman, The influence of bioturbation on iron and sulphur cycling in marine sediments: A model analysis. *Aquat. Geochem.* **22**, 469–504 (2016).
54. S. J. van de Velde, A. W. Dale, S. Arndt, Bioturbation and the δ^{56}Fe signature of dissolved iron fluxes from marine sediments. *R. Soc. Open Sci.* **10**, 220010 (2023).
55. F. J. R. Meysman, B. P. Boudreau, J. J. Middelburg, Modeling reactive transport in sediments subject to bioturbation and compaction. *Geochim. Cosmochim. Acta* **69**, 3601–3617 (2005).
56. C. Meile, P. Berg, P. Van Cappellen, K. Tuncay, Solute-specific pore water irrigation: Implications for chemical cycling in early diagenesis. *J. Mar. Res.* **63**, 601–621 (2005).
57. A. Fick, Uber diffusion. *Ann. Phys. Rehabil. Med.* **94**, 59–86 (1855).
58. K. Soetaert, T. Petzoldt, F. J. R. Meysman, marelac: Tools for Aquatic Sciences R package version 2.1. 2010.
59. B. P. Boudreau, The diffusive tortuosity of fine-grained unlithified sediments. *Geochim. Cosmochim. Acta* **60**, 3139–3142 (1996).
60. F. J. R. Meysman, B. P. Boudreau, J. J. Middelburg, When and why does bioturbation lead to diffusive mixing? *J. Mar. Res.* **68**, 881–920 (2010).
61. D. J. P. Swift, J. K. Stull, A. W. Niedoroda, C. W. Reed, G. T. F. Wong, Contaminant dispersal on the Palos Verdes continental margin II. Estimates of the biodiffusion coefficient, DB, from composition of the benthic infaunal community. *Sci. Total Environ.* **179**, 91–107 (1996).
62. B. P. Boudreau, Mean mixed depth of sediments: The wherefore and the why. *Limnol. Oceanogr.* **43**, 524–526 (1998).
63. J. J. Middelburg. "Marine carbon biogeochemistry" in *Marine Carbon Biogeochemistry. A Primer for Earth System Scientists* (Springer Nature Switzerland AG, 2019).
64. B. P. Boudreau, On the equivalence of nonlocal and radial-diffusion models for porewater irrigation. *J. Mar. Res.* **42**, 731–735 (1984).
65. S. Emerson, R. Jahnke, D. Heggie, Sediment-water exchange in shallow water estuarine sediments. *J. Mar. Res.* **42**, 709–730 (1984).
66. E. Kristensen, H. Røy, K. Debrabant, T. Valdemarsen, Carbon oxidation and bioirrigation in sediments along a Skagerrak–Kattegat–Belt Sea depth transect. *Mar. Ecol. Prog. Ser.* **604**, 33–50 (2018).
67. S. Arndt, B. B. Jørgensen, D. E. LaRowe, J. J. Middelburg, R. D. Pancost, P. Regnier, Quantifying the degradation of organic matter in marine sediments: A review and synthesis. *Earth Sci. Rev.* **123**, 53–86 (2013).
68. F. J. R. Meysman, J. J. Middelburg, P. M. J. Herman, C. H. R. Heip, Reactive transport in surface sediments. II. Media: An object-oriented problem-solving environment for early diagenesis. *Comput. Geosci.* **29**, 301–318 (2003).
69. A. D. Rijnsdorp, J. Depestele, P. Molenaar, O. R. Eigaard, A. Ivanović, F. G. O'Neill, Sediment mobilization by bottom trawls: A model approach applied to the Dutch North Sea beam trawl fishery. *ICES J. Mar. Sci.* **78**, 1574–1586 (2021).
70. F. G. O'Neill, K. Summerbell, The mobilisation of sediment by demersal otter trawls. *Mar. Pollut. Bull.* **62**, 1088–1097 (2011).
71. F. G. O'Neill, K. D. Summerbell, The hydrodynamic drag and the mobilisation of sediment into the water column of towed fishing gear components. *J. Mar. Syst.* **164**, 76–84 (2016).
72. X. Durrieu de Madron, B. Ferré, G. Le Corre, C. Grenz, P. Conan, M. Pujo-Pay, R. Buscail, O. Bodiot, Trawling-induced resuspension and dispersal of muddy sediments and

dissolved elements in the Gulf of Lion (NW Mediterranean). *Cont. Shelf Res.* **25**, 2387–2409 (2005).
73. R. R. McCandliss, S. E. Jones, M. Hearn, R. Latter, C. F. Jago, Dynamics of suspended particles in coastal waters (southern North Sea) during a spring bloom. *J. Sea Res.* **47**, 285–302 (2002).
74. L. M. Mayer, D. F. Schick, R. H. Findlay, D. L. Rice, Effects of commercial dragging on sedimentary organic matter. *Mar. Environ. Res.* **31**, 249–261 (1991).
75. C. Morys, V. Brüchert, C. Bradshaw, Impacts of bottom trawling on benthic biogeochemistry in muddy sediments: Removal of surface sediment using an experimental field study. *Mar. Environ. Res.* **169**, 105384 (2021).
76. C. R. Pitcher, J. G. Hiddink, S. Jennings, J. Collie, A. M. Parma, R. Amoroso, T. Mazor, M. Sciberras, R. A. McConnaughey, A. D. Rijnsdorp, M. J. Kaiser, P. Suuronen, R. Hilborn, Trawl impacts on the relative status of biotic communities of seabed sedimentary habitats in 24 regions worldwide. *Proc. Natl. Acad. Sci. U.S.A.* **119**, e2109449119 (2022).
77. R Core Team. *R: A Language and Environment for Statistical Computing* (R Foundation for Statistical Computing, 2017).
78. B. P. Boudreau, A method-of-lines code for carbon and nutrient diagenesis in aquatic sediments. *Comput. Geosci.* **22**, 479–496 (1996).
79. K. Soetaert, F. Meysman, Reactive transport in aquatic ecosystems: Rapid model prototyping in the open source software R. *Environ. Model. Software* **32**, 49–60 (2012).
80. K. Soetaert, T. Petzoldt, R. W. Setzer, Package deSolve: Solving initial value differential equations in R. *J. Stat. Softw.* **33**, 1–25 (2010).
81. P. Brown, G. Byrne, A. Hindmarsh, VODE, a variable-coefficient ODE solver. *SIAM J. Sci. Stat. Comput.* **10**, 1038–1051 (1989).
82. Shom; https://services.data.shom.fr/geonetwork/srv/eng/catalog.search#/metadata/HOM_GEOL_SEDIM_MONDIALE.xml.
83. T. P. Boyer, H. E. Garcia, R. A. Locarnini, M. M. Zweng, A. V. Mishonov, J. R. Reagan, K. A. Weathers, O. K. Baronova, C. R. Paver, D. Seidov, I. V. Smolyar, World Ocean Atlas 2018. https://www.ncei.noaa.gov/archive/accession/NCEI-WOA18.
84. O. Eigaard, F. Bastardie, M. Breen, G. Dinesen, N. Hintzen, P. Laffargue, L. Mortensen, J. R. Nielsen, H. Nilsson, F. O'Neill, H. Polet, D. G. Reid, A. Sala, M. Sköld, C. Smith, T. Sorensen, O. Tully, M. Zengin, A. Rijnsdorp, Estimating seabed pressure from demersal trawls, seines, and dredges based on gear design and dimensions. *ICES J. Mar. Sci.* **73**, i27–i43 (2016).
85. A. W. Dale, L. Nickelsen, F. Scholz, C. Hensen, A. Oschlies, K. Wallmann, A revised global estimate of dissolved iron fluxes from marine sediments. *Global Biogeochem. Cycles* **29**, 691–707 (2015).
86. J. L.Sarmiento, N. Gruber. *Ocean Biogeochemical Dynamics* (Princeton Univ. Press, 2006).
87. H. Brenner, U. Braeckman, M. Le Guitton, F. J. R. Meysman, The impact of sedimentary alkalinity release on the water column CO_2 system in the North Sea. *Biogeosciences* **13**, 841–863 (2016).
88. D. J. Burdige, R. C. Zimmerman, X. Hu, Rates of carbonate dissolution in permeable sediments estimated from pore-water profiles: The role of sea grasses. *Limnol. Oceanogr.* **53**, 549–565 (2008).
89. L. M. Walter, E. A. Burton, Dissolution of recent platform carbonate sediments in marine pore fluids. *Am. J. Sci.* **290**, 601–643 (1990).
90. A. J. Andersson, N. R. Bates, F. T. Mackenzie, Dissolution of carbonate sediments under rising pCO_2 and ocean acidification: Observations from Devil's Hole, Bermuda. *Aquat. Geochem.* **13**, 237–264 (2007).
91. A. Mucci, B. Sundby, M. Gehlen, T. Arakaki, S. Zhong, N. Silverberg, The fate of carbon in continental shelf sediments of eastern Canada: A case study. *Deep-Sea Res. II Top. Stud. Oceanogr.* **47**, 733–760 (2000).
92. W. M. Berelson, W. M. Balch, R. Najjar, R. A. Feely, C. Sabine, K. Lee, Relating estimates of $CaCO_3$ production, export, and dissolution in the water column to measurements of $CaCO_3$ rain into sediment traps and dissolution on the sea floor: A revised global carbonate budget. *Global Biogeochem. Cycles* **21**, (2007).
93. G. G. Laruelle, H. H. Dürr, R. Lauerwald, J. Hartmann, C. P. Slomp, N. Goossens, P. A. G. Regnier, Global multi-scale segmentation of continental and coastal waters from the watersheds to the continental margins. *Hydrol. Earth Syst. Sci.* **17**, 2029–2051 (2013).
94. D. J. Burdige, Preservation of organic matter in marine sediments: Controls, mechanisms, and an imbalance in sediment organic carbon budgets? *Chem. Rev.* **107**, 467–485 (2007).

Acknowledgments
Funding: This work was supported by Belgian Federal Science Policy Office, grant no. RV/21/DEHEAT (S.J.v.d.V. and F.J.R.M.) and FWO, junior postdoctoral fellowship, project no. 1241724 N (A.H.). **Author contributions:** Writing—original draft: S.J.v.d.V. Conceptualization: S.J.v.d.V. and F.J.R.M. Investigation: S.J.v.d.V. and A.H. Writing—review and editing: S.J.v.d.V., A.H., and F.J.R.M. Methodology: S.J.v.d.V. Funding acquisition: S.J.v.d.V., A.H., and F.J.R.M. Data curation: S.J.v.d.V. and A.H. Validation: S.J.v.d.V. Supervision: S.J.v.d.V. and F.J.R.M. Formal analysis: S.J.v.d.V. Software: S.J.v.d.V. Project administration: S.J.v.d.V., A.H., and F.J.R.M. Visualization: S.J.v.d.V. **Competing interests:** The authors declare that they have no competing interests. **Data and materials availability:** All data needed to evaluate the conclusions in the paper are present in the paper and/or the Supplementary Materials. The code for the diagenetic model used in this paper is tagged as v.1.0.0 and is available at: https://doi.org/10.5281/zenodo.14020804.

Submitted 17 April 2024
Accepted 25 February 2025
Published 28 March 2025
10.1126/sciadv.adp9112